

Article

Effects of Sn and Sb on the Hot Ductility of Nb+Ti Microalloyed Steels

Chunyu He, Jianguang Wang ^{*}, Yulai Chen, Wei Yu  and Di Tang

National Engineering Research Center for Advanced Rolling Technology, University of Science and Technology Beijing, Beijing 100083, China; chunyuhe@163.com (C.H.); yulaic@ustb.edu.cn (Y.C.); yuwei@nercar.ustb.edu.cn (W.Y.); tangdi@nercar.ustb.edu.cn (D.T.)

* Correspondence: g20189146@xs.ustb.edu.cn; Tel.: +86-185-1859-2018

Received: 20 November 2020; Accepted: 14 December 2020; Published: 16 December 2020



Abstract: Referencing the composition of a typical Nb+Ti microalloyed steel (Q345B), two kinds of steels, one microalloyed with Sn and Sb, and the other one only microalloyed with Sb were designed to study the effects of Sn and Sb on the hot ductility of Nb+Ti microalloyed steels. The Gleeble-3500 tester was adopted to determine the high-temperature mechanical properties of the two test steels. Fracture morphologies, microstructures and interior precipitation status were analyzed by SEM, CLSM (Confocal laser scanning microscope) and EDS, respectively. Results revealed that within the range of 950–650 °C, there existed the ductility trough for the two steels, which were mainly attributed to the precipitation of TiN and Nb (C, N). Additionally, precipitation of Sn and Sb were not observed in this research and the hot ductility was not affected by the addition of Sn and Sb, as compared with the Nb+Ti microalloyed steel. Therefore, addition of a small amount of Sn and Sb (≤ 0.05 wt.%) to the Nb+Ti microalloyed steel is favorable due to the improvement on corrosion resistance.

Keywords: microalloyed steel; hot ductility; precipitation; phase transition; microstructure

1. Introduction

Hot ductility metal materials can have a great impact on continuous casting, rolling, and other processes. It is directly related to alloy composition, heating and cooling conditions, sampling direction of the tensile plate, strain rate, and inclusion [1–6]. Researchers have done extensive research on the continuous casting of steel. However, some industrial problems still exist, such as surface defects prone to lateral and angular cracks [5–7]. Additionally, the addition of microalloys Nb, Ti, V, and other elements is regarded as the main reason leading to these problems [8–10].

According to extensive previous reports, hot ductility curves of microalloyed steels obtained by the high-temperature tensile tests have obvious ductility troughs, and brittle regions occur at about 700–1000 °C [8,11,12]. For steels containing Ti and Nb, Xie, You et al. [13] believed that fine Ti, Nb (C, N) particles can be precipitated near the austenite grain boundary at temperatures above 1000 °C, and the precipitates may always exist stably. These fine precipitates pinned the grain boundaries and prevented the occurrence of dynamic recrystallization [9,14,15], which reduced the ductility of the steels ultimately. On the other hand, the addition of Sn and Sb can significantly improve the corrosion resistance of microalloyed steels [16–18]. Ahn, SooHoon, et al. [19] found that SnO₂ and Sb₂O₅, the protective corrosion products produced by microalloyed steels containing Sn and Sb in acid chloride corrosion media, can act as inhibitors of anode reaction. Moreover, the Sn and Sb elements can also work synergistically with Cu to form a continuous and dense Sn-Sb-Cu oxide layer to protect the substrate [16,18,20]. However, it was reported that the additional content of Sn and Sb should

be strictly controlled, or else it may be converted into the unfavorable elements for the toughness of high-strength steel [21].

This paper aims to study the effect of Sn and Sb on the hot ductility of a typical Nb+Ti microalloyed steel (Q345B). Results fully revealed the high-temperature mechanical properties of the designed steels, and related discussion on the fracture morphology and the precipitation status can provide important guidance for the improvement of the actual production process.

2. Experimental

2.1. Experimental Materials

The samples taken in this research are ingots smelted in a laboratory hollow induction furnace. The chemical composition of the experimental steel (Sb+Sn steel and Sb steel) and Q345B steel [22] are as shown in Table 1. After forging, specimens ($\Phi 4$ mm \times 10 mm) were manufactured to conduct the thermal expansion test in the dilatometer-DIL 805 (BÄHR THERMOANALYSE GMBH, Hüllhorst, Germany), and specimens $\Phi 10$ mm \times 120 mm in size were manufactured for the high-temperature tensile test. The processing scheme is presented in Figure 1.

Table 1. Chemical composition of two experimental steels and Q345B (wt.%).

Steel	C	Si	Mn	S	P	Cu+Cr+Ni	Sn	Sb	Al	Nb	Ti	N
Sb+Sn steel	0.062	0.25	0.89	0.003	0.003	1.5–1.9	0.043	0.050		0.039	0.026	0.004
Sb steel	0.083	0.26	0.91	0.006	0.003	1.5–1.9		0.050		0.044	0.025	0.004
Q345B	0.17	0.193	1.438	0.015	0.018				0.028	0.025	0.012	0.004

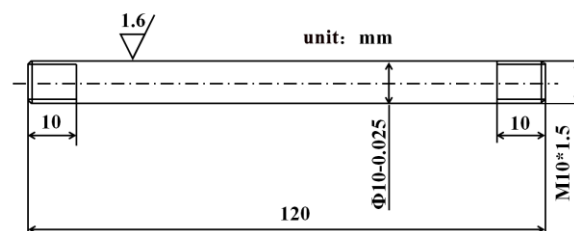


Figure 1. Shape of specimens for hot tensile tests.

The schematic diagram of the specimens after the tensile test is shown in Figure 2a. The cylindrical samples were cut transversely to obtain samples with a length of 10 mm, as shown in Figure 2b, and then cut transversely at a distance of 3 mm from the fracture, as shown in Figure 2c. Finally, the specimens were mechanically polished and etched using 4% nitric acid ethanol solution to observe microstructures.

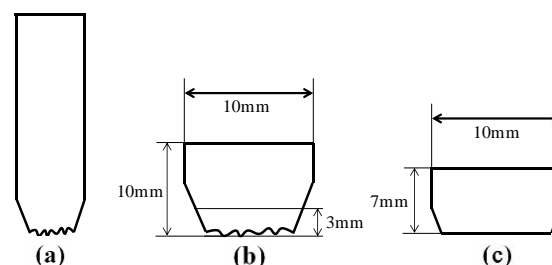


Figure 2. Schematic diagrams of specimen processing showing (a) The specimen after fracture; (b) the specimen near the fracture surface; (c) the final specimen used for microstructure observation.

2.2. Experimental Methods

2.2.1. Thermal Expansion Test

The critical phase transition point of the experimental steels was measured and evaluated by a dilatometer-DIL 805. Specimens were firstly heated to 500 °C at a rate of 10 °C/min and then to 1000 °C at a rate of 3 °C/min, followed by an isothermal process of 3 min, and finally cooled to room temperature at a rate of 3 °C/s. The thermal schedule was depicted in Figure 3a.

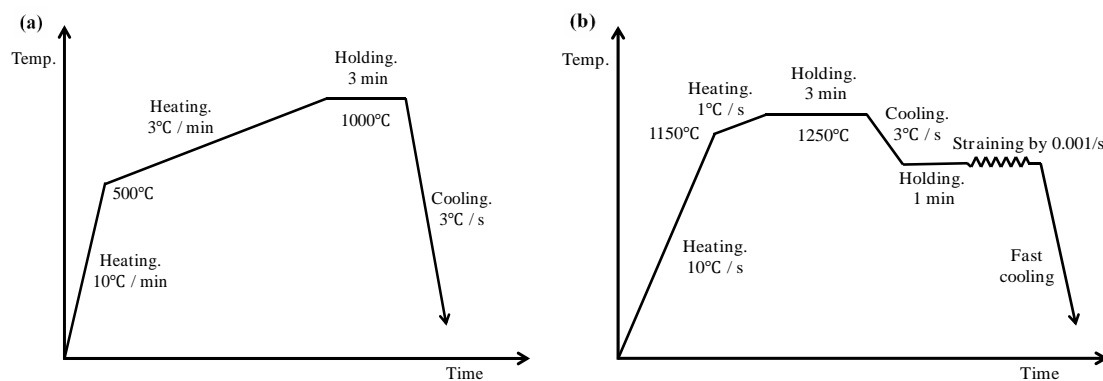


Figure 3. Thermal schedule used to study the critical phase transition and hot ductility. (a) Thermal schedule of the dilatometer test; (b) thermal schedule of the high-temperature tensile test.

2.2.2. High-Temperature Tensile Test

The hot ductility of the experimental steels was measured and evaluated by a high-temperature tensile test, and the experimental equipment was Gleeble-3500 (Dynamic Systems Inc., San Francisco, CA, USA). The sample was firstly heated to 1150 °C at a rate of 10 °C/s, and then the temperature was increased to 1250 °C at a rate of 1 °C/s. Specimens were held at 1250 °C for 3 min to keep the uniformity of the temperature and compositions and also promote the dissolution of precipitates. The specimens were cooled to the testing temperature at a cooling rate of 3 °C/s, and then the heat was held for 1 min before stretching at the strain rate of 10^{-3} /s. The testing temperature range was 650–1250 °C, and the step length was 50 °C. After tension, the specimens were quickly cooled to room temperature to maintain the fracture morphology and microstructures at the testing temperature. The corresponding thermal schedule is shown in Figure 3b.

3. Results

3.1. Critical Transformation Point of Experimental Steels

According to the results of the dilatometer test, we obtained the critical phase transition temperature (Ac_1 , Ac_3 , Ar_1 , Ar_3) [23] of Sb steel $Ac_1 = 762$ °C, $Ac_3 = 865$ °C, $Ar_1 = 709$ °C, $Ar_3 = 764$ °C; and of Sb+Sn steel $Ac_1 = 741$ °C, $Ac_3 = 868$ °C, $Ar_1 = 705$ °C, $Ar_3 = 759$ °C.

3.2. Hot Ductility and Strength

Previous research shows that the continuous casting slab does not crack when the percentage reduction of the area measured by the high-temperature tensile test is above 60% ($Z > 60\%$), and when $Z < 60\%$, on the contrary, the crack sensitivity of the casting slab increases [24,25]. Thus, the 60% percent reduction of the area can be used as a threshold value to divide the high plastic and low plastic zones of steels in this research.

In order to explain the hot ductility characteristics of the two experimental steels more precisely, we compared the hot ductility data of Sb or Sb+Sn modified Nb+Ti microalloyed steels with original steels (Q345B) [22]. Figure 4 shows the relationship between the percentage reduction of area and the

testing temperature of two experimental steels, and Q345B, Ar1, Ac1, Ar3, and Ac3 are the critical transformation points of Sb+Sn steel. It indicates that Q345B has two low plasticity zones (1300–1350 °C and 650–900 °C) in the range of 650 °C to 1350 °C, and a high plasticity zone (900–1300 °C). Obviously, Sb steel and Sb+Sn steel exhibited outstanding plasticity at 1000–1250 °C. In addition, the plasticity of Sb steel and Sb+Sn steel showed a tendency of decreasing first and then increasing at the range from 650 °C to 950 °C, and the lowest valley of the percentage reduction of the area appeared at 750 °C. In general, the hot ductility of the two test steels is similar to that of Q345B.

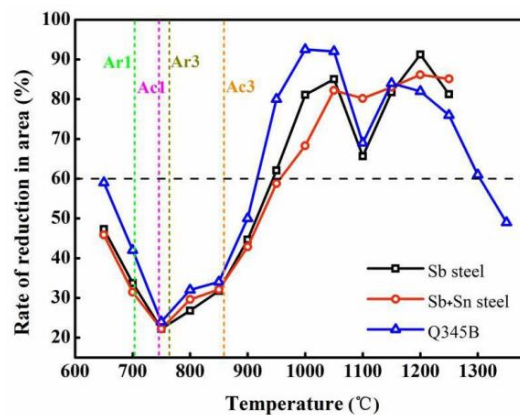


Figure 4. Hot ductility curves.

There are three high-temperature ductility troughs as the temperature rises from 600 °C to the melting points of steel [6,24,26]. The first ductility trough is attributed to S, P, and O elements enriched at the grain boundaries above 1300 °C, and the ductility is reduced due to the inclusion of (Fe, Mn, Si)(S, O) in the dendritic intergranular region. The second ductility trough (which appears at high temperature (800–1300 °C) when the strain rate (higher than 10^{-2} /s) is higher) is related to the strain rate, which usually appears at higher strain rates [27]. The experimental steels did not show the first and second ductility trough in the experimental conditions and temperature range. However, the third ductility trough that generally exists in the range of 700–1000 °C [8,28,29] appeared in the temperature range from 650–950 °C, which can be induced by numerous reasons. It is also strengthened in this research and discussed in detail in the following sections.

Figure 5 shows the relationship between tensile strength and the tensile temperature of three steels. When the maximum stress of the specimens against plastic deformation exceeds the tensile strength, there will be microcracks that affect the quality of the specimens [26]. It can be seen that the tensile strength of Q345B is much lower than that of the two experimental steels below 900 °C, and the performance of steels tends to coincidence when the temperature above 900 °C. Moreover, both of the modified steels present an increase of strength around 1000 °C as compared with Q345B.

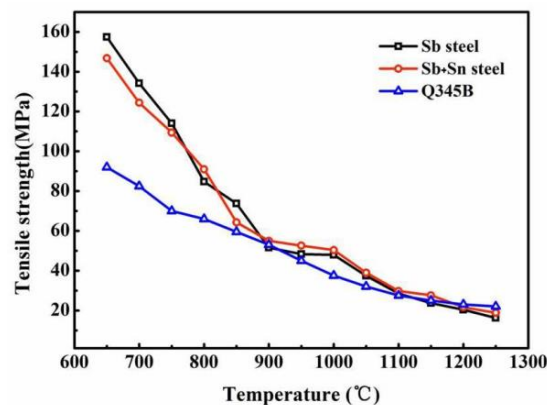


Figure 5. Thermal strength curve.

4. Discussion

4.1. Stress–Strain Behavior

Dynamic recovery and dynamic recrystallization are the two main mechanisms that lead to material softening during high-temperature deformation, and the latter can bring about a more significant softening effect, generally showing obvious stress fluctuations on the high-temperature tensile curve [30,31]. In the process of high-temperature and low-strain-rate deformation, there is also work hardening, and dynamic precipitation strengthening processes, and the softening caused by dynamic recrystallization alternate as the main deformation mechanism will show multipipeak stress on the tensile curve status [32].

Ryan [33] observed that the presence of a stress peak in a constant strain rate flow curve leads to an inflection in the stress dependence of the strain hardening rate, $\theta = (\partial\sigma/\partial\varepsilon)_\varepsilon$. Later, on the basis of considerations of irreversible thermodynamics, the inflections in θ - ε plots in austenitic stainless steels were shown to be due to the initiation of dynamic recrystallization [34,35]. This was subsequently confirmed by the observations in other materials [36]. We find the inflection point from θ - ε plots in the upper right corner of Figure 6a,b, and designate it as the occurrence point of dynamic recrystallization.

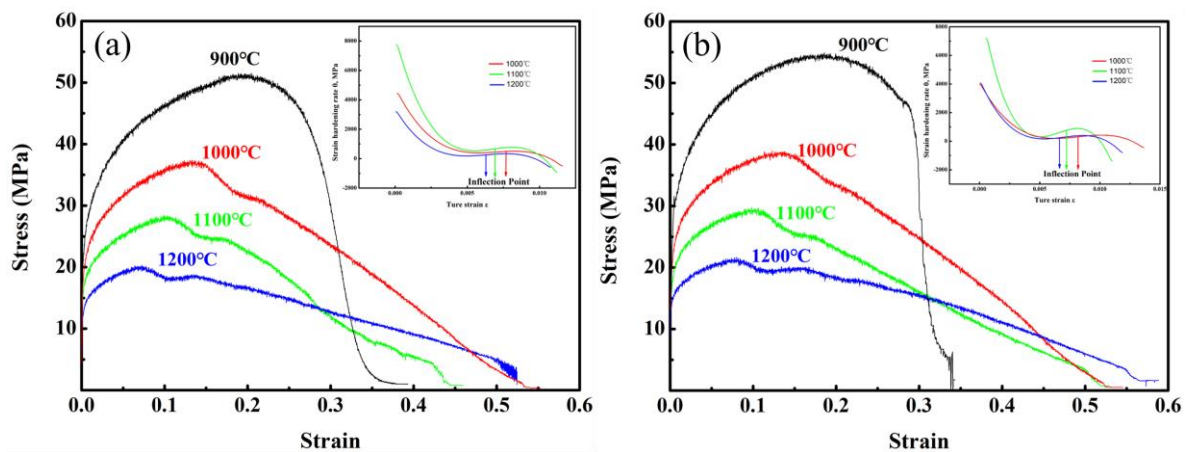


Figure 6. True stress-true strain curve. (a) Sb steel; (b) Sb+Sn steel.

It can be seen from Figure 6 that, as the deformation temperature increases, the strain required for recrystallization softening to occur becomes smaller. The 900 °C tensile curve shows a unimodal shape, indicating that work hardening always occupies the main deformation mechanism at this temperature. The percentage reduction of the area of Sb steel and Sb+Sn steel is higher than 60% in the lower-higher temperature of 950–1250 °C, which is caused by the occurrence of dynamic recrystallization process.

4.2. Influence of Precipitation on Hot Ductility

Matveev et al. [37] believed that the precipitates, inclusions, interstitial impurities, and other factors on the initial grain boundaries were the reasons for the ductility decrease. As shown in Figure 7, the Thermo-Calc (TCFE7 database) software (Stockholm, Sweden) was used to calculate constituents of precipitates and related precipitation order in Sb+Sn steel. The main precipitation elements of the experimental steel were Ti and Nb. Precipitation of Ti appears between 1050 and 1487 °C, and the main precipitates are in the form of TiN. While the precipitation temperature range of Nb is 800–1120 °C, the main precipitates are in the form of Nb (C, N). Therefore, the Nb (C, N) in the experimental steel can be completely dissolved while the original TiN cannot, due to the influence of the experimental heating temperature. When the testing temperature decreases from 950 to 850 °C, the increased content of precipitates (TiN, Nb (C, N)) resulted in increasingly severe grain boundary pinning, which inhibited boundary migration and hindered the occurrence of dynamic recrystallization.

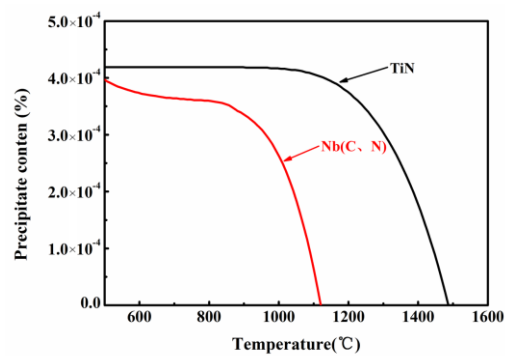


Figure 7. Thermo-Calc software calculates the precipitation order and amount of Sb+Sn steel.

In order to analyze the cause of the worst hot ductility at 750 °C, an energy spectrum analysis is performed on the fracture morphology of Sb+Sn steel. As shown in Figure 8a, there is an empty hole on the fracture surface and a precipitate inside, and the precipitate is determined to be a Ti+Nb carbide, as shown in Figure 8b. However, the diffraction peaks of Sb and Sn are not detected, so the Sn and Sb elements do not produce precipitates, and the phenomenon of pinning grain boundaries is not aggravated. Studies have shown that when the content of Sb and Sn elements is high, they tend to aggregate at the grain boundaries [21]. Figure 9a is an SEM photograph of Sb+Sn steel with obvious grain boundaries. EDS microarea surface scan results show that Sb and Sn elements are evenly distributed in the solid solution in Figure 9b,c.

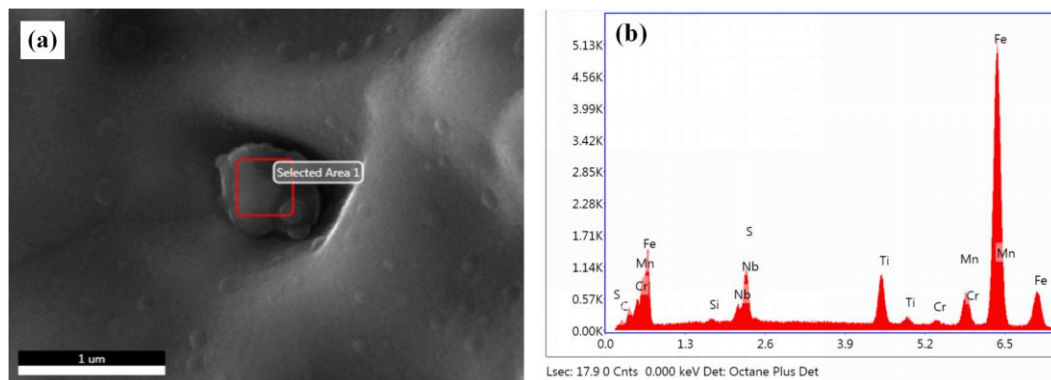


Figure 8. Fracture energy spectrum of Sb+Sn steel at 750 °C. (a) Scanning area; (b) energy spectrum.

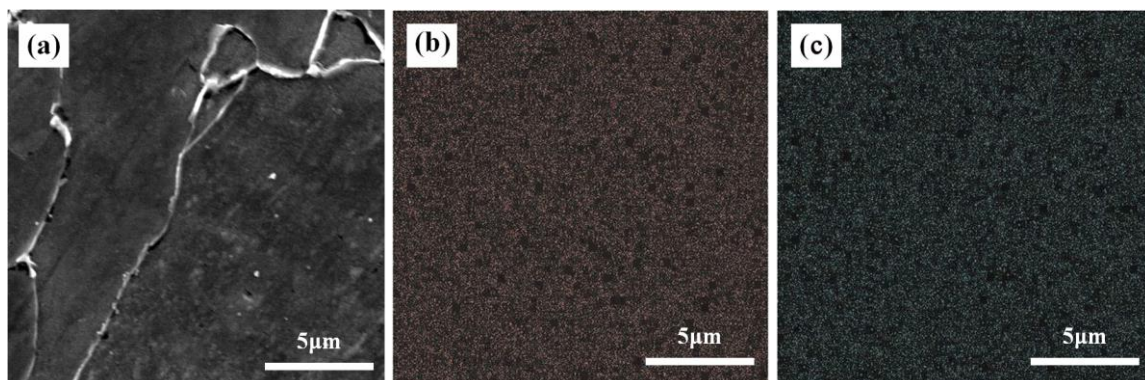


Figure 9. SEM photograph and energy spectrum. (a) Scanning area; (b) Sb energy spectrum; (c) Sn energy spectrum.

However, as can be seen from Figure 4, the percentage reduction of area of the experimental steel is generally lower than that of Q345B especially in the low plastic zone, which is mainly attributed

to the precipitate content. The contents of Ti and Nb in Q345B are 0.012 (wt.%) and 0.025 (wt.%), respectively, and the contents of Ti and Nb in experimental steel are 0.025 (wt.%) and 0.04 (wt.%), respectively. The content of Ti and Nb precipitates in the experimental steel is higher, this weakens the ductility of the steel. It can be seen from Figure 5 that the strength of the experimental steels is significantly higher than Q345B at 1000 °C, which may be due to the precipitation strengthening of Ti+Nb. Based on the above analysis, we believe that adding an appropriate amount of Sb and Sn elements to the experimental steel does not affect the hot ductility.

4.3. Fracture Morphology Analysis and Microstructure

The fracture morphologies of Sb steel and Sb+Sn steel at different tensile temperatures are shown in Figure 10. At a test temperature of 1100 °C, there are a large number of dimples that existed on the fracture surface, as can be seen in Figure 10a,e. Under high-temperature strain, dynamic recrystallization allows the grain boundary to obtain sufficient driving force to migrate. At this time, the migration speed of the grain boundary is higher than the slip speed of the grain boundary, which wraps the already formed grain boundary crack into the grain and reduces the cracking speed at grain boundaries. Interconnection of the cracks in the grain requires a greater external force to cut the whole grain and eventually rupture. Therefore, the occurrence of dynamic recrystallization is conducive to the improvement of hot ductility. As the experimental temperature decreased to 850 °C, the fracture morphology showed obvious cleavage fracture characteristics, as shown in Figure 10b,f. The loss of ductility from 1100 °C to 850 °C can be explained by the precipitates, which provide a pinning effect on the austenite grain boundaries and prevent the recrystallization phenomenon of steel. As shown in Figure 10c,g, the fracture morphology under 750 °C shows a typical brittle fractured smooth block structure. At this temperature, the fine grains at the austenite boundary provide nucleation points, and the ferrite film grows the grain boundary to the intragranular region. As the temperature decreases to 650 °C, the fracture morphology can be seen in Figure 10d,h, and the dimples increase significantly.

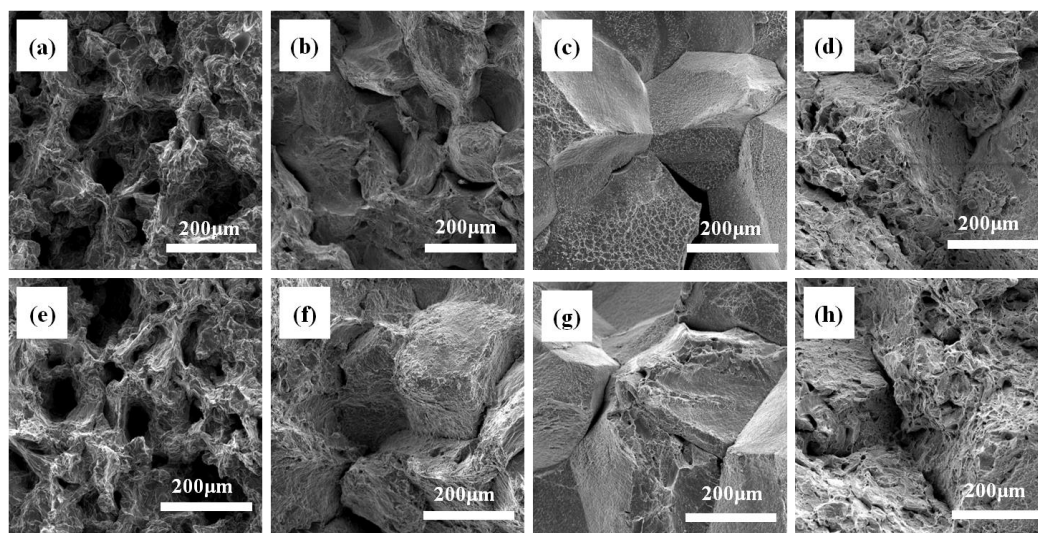


Figure 10. Fracture morphology of Sb steel and Sb+Sn steel at different temperatures. (a) Sb steel-1100 °C; (b) Sb steel-850 °C; (c) Sb steel-750 °C; (d) Sb steel-650 °C; (e) Sb+Sn steel-1100 °C; (f) Sb+Sn steel-850 °C; (g) Sb+Sn steel-750 °C; (h) Sb+Sn steel-650 °C.

Microstructures of the specimens of Sb+Sn steel at different temperatures (1100 °C, 850 °C, 750 °C, and 650 °C) are displayed in Figure 11. The microstructures under 1100 °C and 850 °C are acicular bainite and granular bainite, respectively. At 750 °C, ferrite is formed at the austenite boundary, and the remaining austenite is transformed into bainite. As the temperature decreases to 650 °C,

the hot ductility increases slightly, which is related to the ferrite and pearlite that have undergone phase transformation.

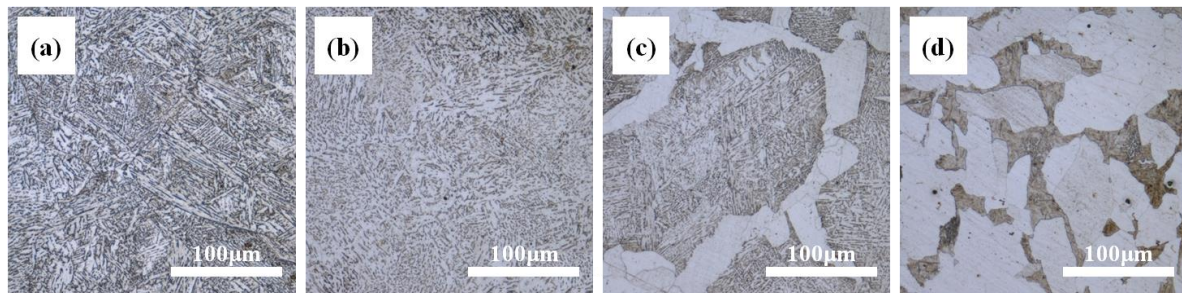


Figure 11. Microstructures of the specimens of Sb+Sn steel at different temperatures. (a) 1100 °C; (b) 850 °C; (c) 750 °C; (d) 650 °C.

4.4. Fracture Mechanism of the Lowest Brittle Valley

A fracture mechanism at 750 °C is involved to further illustrate the fracture mechanism. Primary ferrite has already existed at 750 °C and it is distributed along the austenite grain boundaries. Although both austenite and ferrite have good ductility, when the two phases are present together, ferrite can be considerably softer than austenite, so that most of the strain, therefore, concentrates in these bands, giving low ductility [26]. Then, the mixture of precipitates in the ferrite becomes the core of empty holes formation, and the empty holes grow and accumulate to form microcracks with the increase of strain. Finally, the completely cracked microcracks are the tiny dimples observed on the fracture morphology. Taking the cross-section in the direction of parallel tensile force, the mechanism of microcrack formation is shown in Figure 12.

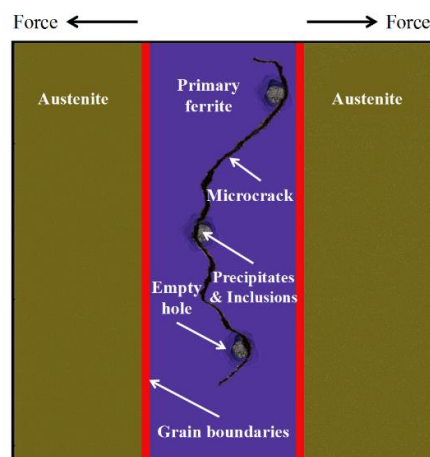


Figure 12. Schematic diagram of the microcrack formation mechanism.

In short, the experimental steel has a ductility trough in the temperature range of 650–950 °C, and the reasons can be concluded as follows: one is the fine precipitates of Ti and Nb pinned to the grain boundary; the other is an austenite-ferrite phase transition. However, the addition of a small number of Sb and Sn microalloying elements does not affect the hot ductility.

5. Conclusions

- (1) Sb steel and Sb+Sn steel did not show the first and second ductility trough in the experimental conditions and temperature range, and the third ductility trough is about 650–950 °C.
- (2) In the high-plasticity zone with the percentage reduction of area of $Z > 60\%$, high temperature and deformation promote the occurrence of dynamic recrystallization, which is beneficial to the

improvement of hot ductility. The third ductility trough, the pinning of the grain boundaries by fine precipitates and the precipitation of primary ferrite along the grain boundaries are responsible for the decrease in hot ductility.

- (3) The $\gamma \rightarrow \alpha$ phase transition temperatures of Sb steel and Sb+Sn steel are 759 °C and 764 °C, respectively. The precipitates of the experimental steel are mainly TiN, Nb (C, N) not Sn and Sb. Adding a small amount of microalloying elements Sb and Sn does not affect the hot plasticity.

Author Contributions: Conceptualization, W.Y. and Y.C.; methodology, C.H. And D.T.; software, J.W.; validation, J.W.; writing—original draft preparation, J.W.; writing—review and editing, C.H., J.W.; funding acquisition, W.Y. All authors have read and agreed to the published version of the manuscript.

Funding: Thanks for the funding of the State Key Project of Research and Development Plan “Steel for Key Components of Railway Vehicles (No. 2017YFB0304600)”.

Conflicts of Interest: The authors declare that they have no known competing financial interests or personal relationships that could have appeared to influence the work reported in this paper.

References

- Sahoo, G.; Singh, B.; Saxena, A. Effect of strain rate, soaking time and alloying elements on hot ductility and hot shortness of low alloy steels. *Mater. Sci. Eng. A* **2018**, *718*, 292–300. [[CrossRef](#)]
- Ma, F.; Wen, G.; Wang, W. Effect of Cooling Rates on the Second-Phase Precipitation and Proeutectoid Phase Transformation of a Nb–Ti Microalloyed Steel Slab. *Steel Res. Int.* **2013**, *84*, 370–376. [[CrossRef](#)]
- Faccoli, M.; Roberti, R. Study of hot deformation behaviour of 2205 duplex stainless steel through hot tension tests. *J. Mater. Sci.* **2013**, *48*, 5196–5203. [[CrossRef](#)]
- Zhang, H.J.; Zhang, L.F.; Wang, Y.D. Effect of Sampling Locations on Hot Ductility of Low Carbon Alloyed Steels. *Steel Res. Int.* **2018**, *89*, 1800052. [[CrossRef](#)]
- Wang, Z.; Ma, W.; Wang, C. Effect of Strain Rate on Hot Ductility of a Duplex Stainless Steel. *Adv. Mater. Sci. Eng.* **2019**, *2019*, 6810326. [[CrossRef](#)]
- Yamamoto, K.; Yamamura, H.; Suwa, Y. Behavior of Non-metallic Inclusions in Steel during Hot Deformation and the Effects of Deformed Inclusions on Local Ductility. *ISIJ Int.* **2011**, *51*, 1987–1994. [[CrossRef](#)]
- Du, C.; Zhang, J.; Wen, J.; Li, Y.; Lan, P. Hot ductility trough elimination through single cycle of intense cooling and reheating for microalloyed steel casting. *Ironmak. Steelmak.* **2016**, *43*, 331–339. [[CrossRef](#)]
- Jang, J.H.; Heo, Y.U.; Lee, C.H.; Bhadeshia, H.K.D.H.; Suh, D.W. Interphase precipitation in Ti–Nb and Ti–Nb–Mo bearing steel. *Mater. Sci. Technol.* **2013**, *29*, 309–313. [[CrossRef](#)]
- Liu, Y.; Du, L.X.; Wu, H.Y.; Misra, R.D.K. Hot Ductility and Fracture Phenomena of Low-Carbon V–Nb–Cr Microalloyed Steels. *Steel Res. Int.* **2019**, *91*, 1900265. [[CrossRef](#)]
- Zhou, Q.; Li, Z.; Wei, Z.S.; Wu, D.; Li, J.Y.; Shao, Z.Y. Microstructural features and precipitation behavior of Ti, Nb and V microalloyed steel during isothermal processing. *J. Iron Steel Res. Int.* **2019**, *26*, 102–111. [[CrossRef](#)]
- Qian, G.; Cheng, G.; Hou, Z. Effect of the Induced Ferrite and Precipitates of Nb–Ti Bearing Steel on the Ductility of Continuous Casting Slab. *ISIJ Int.* **2014**, *54*, 1611–1620. [[CrossRef](#)]
- Lan, P.; Tang, H.; Zhang, J. Hot ductility of high alloy Fe–Mn–C austenite TWIP steel. *Mater. Sci. Eng. A* **2016**, *660*, 127–138. [[CrossRef](#)]
- Xie, Y.; Cheng, G.; Chen, L.; Zhang, Y.; Yan, Q. Characteristics and Generating Mechanism of Large Precipitates in Nb–Ti-microalloyed H13 Tool Steel. *ISIJ Int.* **2016**, *56*, 995–1002. [[CrossRef](#)]
- Vervynckt, S.; Verbeken, K.; Thibaux, P.; Houbaert, Y. Recrystallization–precipitation interaction during austenite hot deformation of a Nb microalloyed steel. *Mater. Sci. Eng. A* **2011**, *528*, 5519–5528. [[CrossRef](#)]
- Carpenter, K.R.; Dippenaar, R.; Killmore, C.R. Hot Ductility of Nb- and Ti-Bearing Microalloyed Steels and the Influence of Thermal History. *Metall. Mater. Trans. A* **2009**, *40*, 573–580. [[CrossRef](#)]
- Nam, N.D.; Kim, M.J.; Jang, Y.W.; Kim, J.G. Effect of tin on the corrosion behavior of low-alloy steel in an acid chloride solution. *Corros. Sci.* **2010**, *52*, 14–20. [[CrossRef](#)]
- Pardo, A.; Merino, M.C.; Carboneras, M.; Coy, A.E.; Arrabal, R. Pitting corrosion behaviour of austenitic stainless steels with Cu and Sn additions. *Corros. Sci.* **2007**, *49*, 510–525. [[CrossRef](#)]

18. Park, S.A.; Kim, S.H.; Yoo, Y.H.; Kim, J.G. Effect of Chloride Ions on the Corrosion Behavior of Low-Alloy Steel Containing Copper and Antimony in Sulfuric Acid Solution. *Met. Mater. Int.* **2015**, *21*, 470–478. [[CrossRef](#)]
19. Ahn, S.; Park, K.J.; Oh, K.; Hwang, S.; Park, B.; Kwon, H.; Shon, M. Effects of Sn and Sb on the Corrosion Resistance of AH 32 Steel in a Cargo Oil Tank Environment. *Met. Mater. Int.* **2015**, *21*, 865–873. [[CrossRef](#)]
20. Pardo, A.; Merino, M.C.; Carboneras, M.; Viejo, F.; Arrabal, R.; Muñoz, J. Influence of Cu and Sn content in the corrosion of AISI 304 and 316 stainless steels in H₂SO₄. *Corros. Sci.* **2006**, *48*, 1075–1092. [[CrossRef](#)]
21. Kameda, J.; McMahon, C.J. The effects of Sb, Sn, and P on the strength of grain boundaries in a Ni-Cr Steel. *Metall. Trans. A* **1981**, *12*, 31–37. [[CrossRef](#)]
22. Liu, J.W.; Wang, C.M.; Yu, L.; Qi, Y.F. Hot Ductility of Q345B low carbon high strength steel. *Nonferrous. Met. Sci. Eng.* **2015**, *6*, 61–67.
23. Song, W.X. *Metal Science*, 2nd ed.; Metallurgical Industry Press: Beijing, China, 1989; pp. 318–319.
24. Chen, D.; Cui, H.; Wang, R. High-Temperature Mechanical Properties of 4.5%Al δ -TRIP Steel. *Appl. Sci.* **2019**, *9*, 5094. [[CrossRef](#)]
25. Fu, J.; Wang, F.M.; Hao, F.; Jin, G.X. High-temperature mechanical properties of near-eutectoid steel. *Int. J. Miner. Metall. Mater.* **2013**, *20*, 829–834. [[CrossRef](#)]
26. Zeng, Y.N.; Sun, Y.H.; Cai, K.K.; Ma, Z.F.; Xi, A. Failure mode and hot ductility of Ti-bearing steel in the brittle zone. *Rev. Metall.* **2013**, *110*, 315–323. [[CrossRef](#)]
27. Mintz, B.; Jonas, J.J. Influence of strain rate on production of deformation induced ferrite and hot ductility of steels. *Mater. Sci. Technol.* **1994**, *10*, 721–727. [[CrossRef](#)]
28. Lanjewar, H.A.; Tripathi, P.; Singhai, M.; Patra, P.K. Hot Ductility and Deformation Behavior of C-Mn/Nb-Microalloyed Steel Related to Cracking during Continuous Casting. *J. Mater. Eng. Perform.* **2014**, *23*, 3600–3609. [[CrossRef](#)]
29. Xie, S.S.; Lee, J.D.; Yoon, U.S.; Yim, C.H. Compression Test to Reveal Surface Crack Sensitivity between 700 and 1100 °C of Nb-bearing and High Ni Continuous Casting Slabs. *ISIJ Int.* **2002**, *42*, 708–716. [[CrossRef](#)]
30. Mejía, I.; Bedolla-Jacuinde, A.; Maldonado, C.; Cabrera, J.M. Hot ductility behavior of a low carbon advanced high strength steel (AHSS) microalloyed with boron. *Mater. Sci. Eng. A* **2011**, *528*, 4468–4474. [[CrossRef](#)]
31. Ghosh, S.; Mula, S. Fracture toughness characteristics of ultrafine grained Nb–Ti stabilized microalloyed and interstitial free steels processed by advanced multiphase control rolling. *Mater. Charact.* **2020**, *159*, 110003. [[CrossRef](#)]
32. Sakai, T.; Jonas, J.J. Dynamic recrystallization: Mechanical and microstructural considerations. *Acta. Metal.* **1984**, *32*, 189–209. [[CrossRef](#)]
33. Ryan, N.D.; McQueen, H.J. Flow stress, dynamic restoration, strain hardening and ductility in hot working of 316 steel. *J. Mater. Process. Technol.* **1990**, *21*, 177–199. [[CrossRef](#)]
34. Mirzadeh, H.; Najafzadeh, A. Prediction of the critical conditions for initiation of dynamic recrystallization. *Mater. Des.* **2010**, *31*, 1174–1179. [[CrossRef](#)]
35. Poliak, E.I.; Jonas, J.J. Initiation of Dynamic Recrystallization in Constant Strain Rate Hot Deformation. *ISIJ Int.* **2007**, *43*, 684–691. [[CrossRef](#)]
36. Kim, S.I.; Lee, Y.; Byon, S.M. Study on constitutive relation of AISI 4140 steel subject to large strain at elevated temperatures. *J. Mater. Process. Technol.* **2003**, *140*, 84–89. [[CrossRef](#)]
37. Matveev, M.A.; Kolbasnikov, N.G.; Kononov, A.A. Causes of High Temperature Ductility Trough of Microalloyed Steels. *Trans. Indian Inst. Met.* **2017**, *70*, 2193–2204. [[CrossRef](#)]

Publisher’s Note: MDPI stays neutral with regard to jurisdictional claims in published maps and institutional affiliations.



© 2020 by the authors. Licensee MDPI, Basel, Switzerland. This article is an open access article distributed under the terms and conditions of the Creative Commons Attribution (CC BY) license (<http://creativecommons.org/licenses/by/4.0/>).